

---

# Description of a Prototype Emission-Transmission Computed Tomography Imaging System

Thomas F. Lang, Bruce H. Hasegawa, Soo Chin Liew\*, J. Keenan Brown, Stephen C. Blankespoor, Susan M. Reilly, Eric L. Gingold, and Christopher E. Cann

*Department of Radiology and Bioengineering Graduate Group, University of California, San Francisco, California*

---

We have developed a prototype imaging system that can perform simultaneous x-ray transmission CT and SPECT phantom studies. This system employs a 23-element high-purity-germanium detector array. The detector array is coupled to a collimator with septa angled toward the focal spot of an x-ray tube. During image acquisition, the x-ray fan beam and the detector array move synchronously along an arc pivoted at the x-ray source. Multiple projections are obtained by rotating the object, which is mounted at the center of rotation of the system. The detector array and electronics can count up to  $10^6$  cps/element with sufficient energy-resolution to discriminate between x-rays at 100–120 kVp and gamma rays from  $^{99m}\text{Tc}$ . We have used this device to acquire x-ray CT and SPECT images of a three-dimensional Hoffman brain phantom. The emission and transmission images may be superimposed in order to localize the emission image on the transmission map.

**J Nucl Med 1992; 33:1881–1887**

---

Two major technical problems have limited the capability of SPECT to quantify the uptake of radionuclide in a region of interest (ROI) within a slice of tissue. First, SPECT images are noise-limited, have poor spatial resolution and often lack anatomic landmarks, resulting in poor anatomic localization and making it difficult to define ROI borders for uptake quantification (1). Second, the nonuniform attenuation of gamma-ray photons by surrounding tissues causes visual distortions and quantitative errors in reconstructed SPECT images (2).

A variety of solutions have been proposed, most of which focus on correlating the functional SPECT image with anatomic data from transmission CT or MRI. Attempts to improve localization of uptake have centered on

merging SPECT or PET images in three dimensions with data sets from x-ray CT or MRI scans (3–5). Such techniques appear to show promise for a range of applications in brain imaging, including radiation therapy planning, Alzheimer's disease, strokes and head trauma (6). Attempts to compensate for nonuniform attenuation have involved acquiring sequential or simultaneous transmission CT scans with external radionuclide point or sheet sources mounted on the gamma camera, thus measuring the distribution of attenuation coefficients in the volume of interest. Incorporation of these attenuation maps into the SPECT reconstruction have yielded significant improvements in both image quality and quantification of uptake (7,8).

Over the past few years, we have developed a different approach to correlating SPECT with anatomic data. A principal result of this work has been the development of a prototype imaging system, designed for phantom studies, that can perform simultaneous SPECT and x-ray CT. Our device, the Emission-Transmission CT (ETCT) system, employs an array of high-purity germanium (HPGe) detectors in conjunction with fast pulse-counting electronics to simultaneously detect and energy-resolve x-ray photons from an external source and higher-energy gamma-ray photons from an internally administered radionuclide source. With the high photon flux available from an x-ray tube, it is possible to obtain transmission CT images with spatial resolution of 1 mm or better, revealing morphological details which may not be visible in radionuclide CT. One feature of this system is that the emission and transmission data are acquired with the same detector and reconstructed with the same geometry, thus allowing the SPECT image to be registered on the x-ray CT map. Moreover, by utilizing the techniques of dual-energy transmission CT, it is possible to derive an energy-corrected attenuation map which may be directly incorporated into an iterative SPECT reconstruction technique, thus improving SPECT quantitation. In this paper, we describe this prototype system and present initial results from phantom studies. We believe that these results, as well as those from future studies, can shed light on the capabilities of a future clinical ETCT system.

---

Received Feb. 11, 1992; revision accepted Jun. 4, 1992.

For reprints contact: Thomas F. Lang, PhD, UCSF Physics Research Lab, 389 Oyster Point Blvd., South San Francisco, CA. 94080.

\* Current address: Department of Physics, National University of Singapore.

## MATERIALS AND METHODS

### System Description

Although a detailed description of the ETCT system components has been previously published (9), a brief summary of the most important features of the device (Fig. 1) is as follows. The ETCT prototype was designed to simulate a clinical emission-transmission brain scanner having a third-generation x-ray CT detector geometry and a 30° x-ray fan-beam encompassing a reconstruction circle with a 22-cm diameter (10). The prototype instrument contains a detector array consisting of a single HPGe crystal segmented into 23 2-mm elements. The HPGe detector array is equipped with a tantalum collimator with septa focused to the focal spot of a low-power x-ray tube, providing spatial localization for SPECT and scatter rejection for x-ray CT. The detectors have shown full-spectrum count rate capabilities exceeding  $10^6$  cps/channel, and measurements at count rates of  $6 \times 10^5$  cps/channel have demonstrated energy resolutions of 8 keV FWHM for 60-keV photon energies (11). As shown in Figure 2, this is sufficient to discriminate between 140-keV gamma-ray photons from  $^{99m}\text{Tc}$  and x-ray photons produced at tube potentials of 100 or 120 kVp. Moreover, since the data acquisition system supports two energy windows per channel, it is possible to acquire simultaneous emission-transmission data or dual-energy x-ray data. Finally, as displayed in Figure 3, the system acquires CT data by translating the detector array in increments of one-half detector width along a 30° arc pivoted at the x-ray source. At each detector position, a complete set of projection angles is obtained by rotating the object on a shaft which defines the center of rotation of the system. Since the detector data comprising one projection angle is thus acquired over the duration of the whole scan, the count rate response of the data acquisition system must remain stable within Poisson statistics over the duration of the scan. Long-term (5 days) tests with a  $^{153}\text{Gd}$  source found count rate instabilities of 0.045%, which were in good agreement with a value of 0.039% predicted from Poisson statistics alone (11) and which fall well within the Poisson noise envelope associated with our x-ray CT data.

### System Performance Studies

**Radiographic Spatial Resolution.** We have acquired radiographic spatial resolution data using x-ray tube settings of 120 kVp and 4 mA, with 1 mm gadolinium filtration and with energy

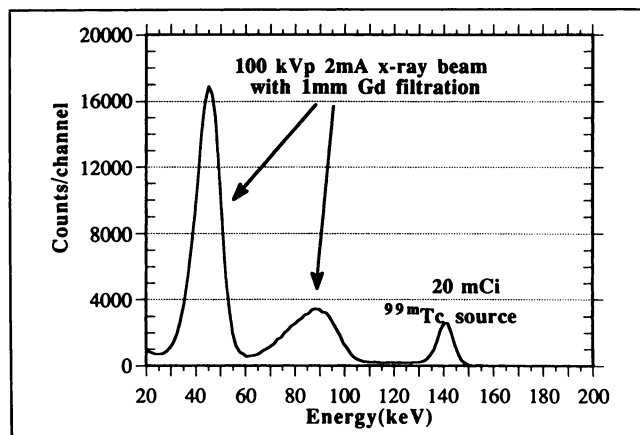


**FIGURE 2.** Energy spectrum obtained with x-ray tube settings of 100 kVp and 2 mA. The x-ray beam is filtered with 1 mm of Gd, and a 740 MBq  $^{99m}\text{Tc}$  source is resting on the detector aperture.

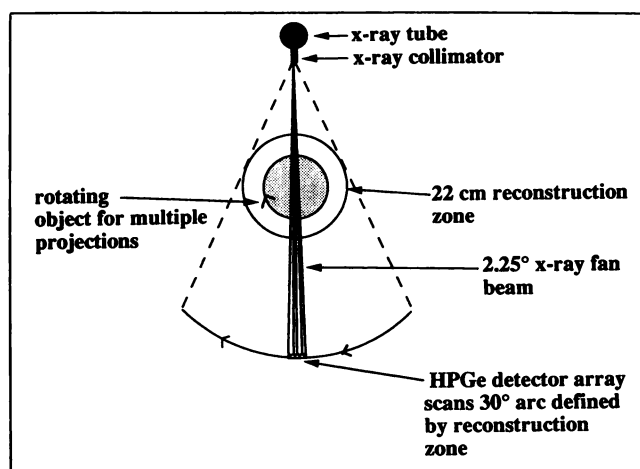


**FIGURE 3.** A diagram of the ETCT scan geometry. The 23-element HPGe detector moves in an arc which encompasses the reconstruction zone. Multiple projections are obtained by rotating the object.

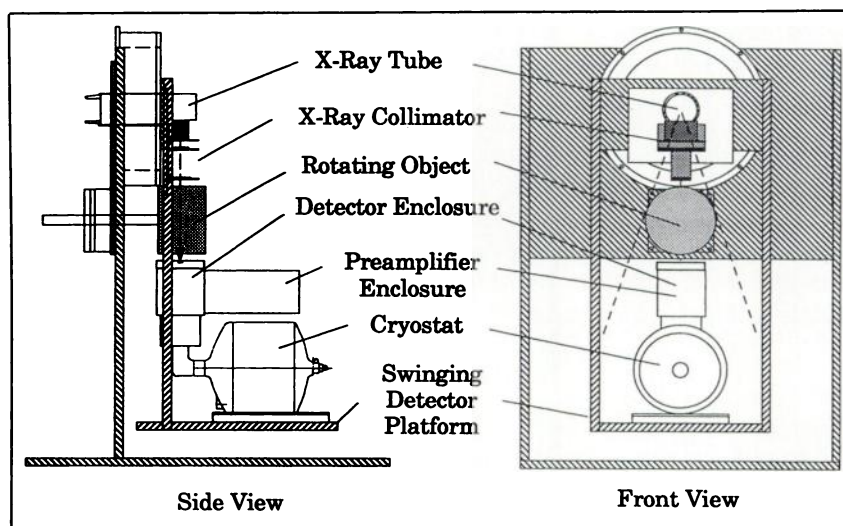


**FIGURE 1.** A drawing of the assembled ETCT system.

windows encompassing each peak of the bi-modal filtered x-ray energy spectrum. Projection data were acquired with 180 views across a 360° rotation, moving the detector array in 1-mm increments across a 16.8° arc encompassing the diameter of the resolution phantom. The x-ray projection data were subsequently convolved with a Ramachandran-Lakshminarayan (12) convolution kernel and reconstructed onto a 256 × 256 matrix using a backprojection algorithm developed for the curved ETCT detector geometry (13).

**SPECT Spatial Resolution.** Emission images were acquired of a 20-cm-diameter SPECT hot lesion pattern (Nuclear Associates, Carle Place, NY). The phantom was filled with de-ionized water containing 740 MBq of [<sup>99m</sup>Tc]pertechnetate. During data acquisition, the detector array sampled a 30° fan angle with 1-mm detector increments; at each detector array position, the phantom was sampled at 2° intervals across a 360° rotation. The emission data were acquired with a 20-keV wide energy window encompassing the 140-keV gamma-ray peak. Subsequently, the data were corrected for decay of the radionuclide during the 4-hr scan and were reconstructed using a maximum likelihood expectation-maximization (ML-EM) algorithm adapted to the ETCT system geometry (8). This ML-EM reconstruction incorporated a circular and uniform ( $\mu = 0.15 \text{ cm}^{-1}$ ) attenuation map having a diameter equal to that measured from the resolution phantom and centered within the reconstruction zone. Values outside the circular region were set equal to zero. In this study, we did not incorporate object-specific attenuation maps derived from correlated dual-energy x-ray CT, although preliminary work on this concept is now underway (9).

### Emission-Transmission Studies of a Hoffman Brain Phantom

We acquired x-ray CT and SPECT images of a three-dimensional Hoffman brain phantom (Data Spectrum Corporation, Durham, NC). This phantom was filled with de-ionized water containing 740 MBq of [<sup>99m</sup>Tc]pertechnetate. The phantom was mounted on the ETCT system, and two imaging studies were then performed, the first recording only radionuclide data and the second recording both radionuclide and radiographic data. These measurements were performed separately in order to evaluate the effect on the simultaneously acquired SPECT image of x-ray pile-up counts introduced into the radionuclide energy window by the high x-ray photon flux. In both studies, a 20-keV radionuclide energy window was centered at 140 keV and the detector array sampled a 30° fan angle in 1-mm detector increments, with 180 projections and a 360° phantom rotation. The simultaneous emission-transmission study, which employed an additional x-ray energy window between 60 and 120 keV, was performed with the x-ray tube at 100 kVp and 4 mA, with 1 mm Gd filtration. These x-ray settings produced  $5 \times 10^9$  counts in the x-ray window and  $4 \times 10^7$  counts in the radionuclide energy window, corresponding to both radionuclide decay and x-ray pile-up (compared to  $4 \times 10^6$  counts for the SPECT-only acquisition). Following the two studies, the separately acquired radionuclide and the simultaneously acquired x-ray data were reconstructed with ML-EM and convolution backprojection algorithms respectively.

It was necessary to correct the simultaneously acquired radionuclide data for x-ray pile-up. Although the total pile-up signal was ten times that of the radionuclide, the pile-up signal was significant only when the x-ray fan beam was outside or in the

peripheral 2 cm of the phantom. This contribution was estimated and subtracted using a simple calibration procedure in which the x-ray fan beam was stepped across a water-filled uniformity phantom and the count rates in the x-ray and radionuclide windows were recorded in the absence of radionuclide. Thus, the pile-up rate was measured as a function of the x-ray count rate, which varied as the x-ray beam traversed the phantom. Because the x-ray energy window was set between 60 and 120 keV, and a pile-up event could be represented as the detection of two independent photons within this energy range, the pile-up counts were expected to vary as the square of the x-ray counts. The results are displayed in Figure 4, where the solid curve drawn through the data points is a second order polynomial given by:

$$N_p = 0.311 - (7.28 \times 10^{-4} \cdot N_x) + (5.98 \times 10^{-8} \cdot N_x^2), \quad \text{Eq. 1}$$

where  $N_p$  and  $N_x$  are the pile-up and x-ray counts, respectively. With this calibration curve, which predicted the pile-up counts within statistical error of the experimental values, it was possible to use the x-ray projection data to estimate the pile-up contribution to each sample of the simultaneously-acquired radionuclide data. The corrected data, which contained  $2 \times 10^6$  radionuclide counts, could then be adjusted for <sup>99m</sup>Tc decay and reconstructed with the ML-EM algorithm described above.

### RESULTS

Images of radiographic and radionuclide resolution phantoms are respectively displayed on the left and right in Figure 5. In the x-ray image, it is possible to resolve the second row of holes from the bottom, which are 1.25 mm in diameter and spaced 1.25 mm apart. In the SPECT image, it is possible to resolve the pair of lesions which are 0.6 cm in diameter and spacing.

Images of the three-dimensional Hoffman brain phantom are displayed in Figure 6. The upper left-hand figure is an x-ray CT image of the phantom obtained with the x-ray tube off. This image was reconstructed from  $4 \times 10^6$  photons. The bottom figure shows the separately acquired SPECT image overlaid in transparent color on the x-ray CT gray-scale image. The program employed to superim-

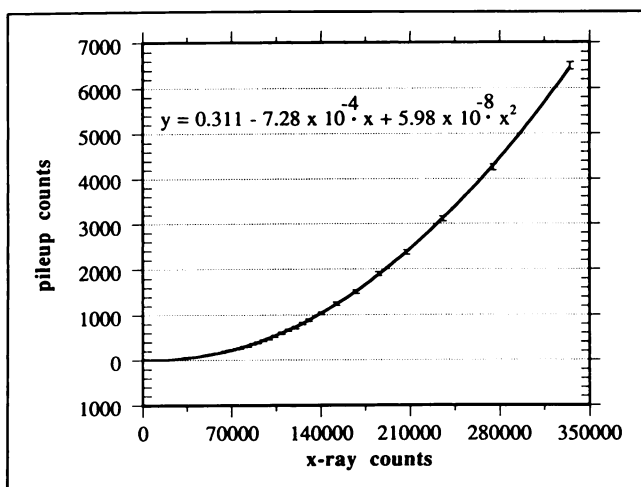


**FIGURE 4.** Plot of pileup counts in the radionuclide energy window as a function of counts in the x-ray window. Line through data points is a second-order polynomial fit.

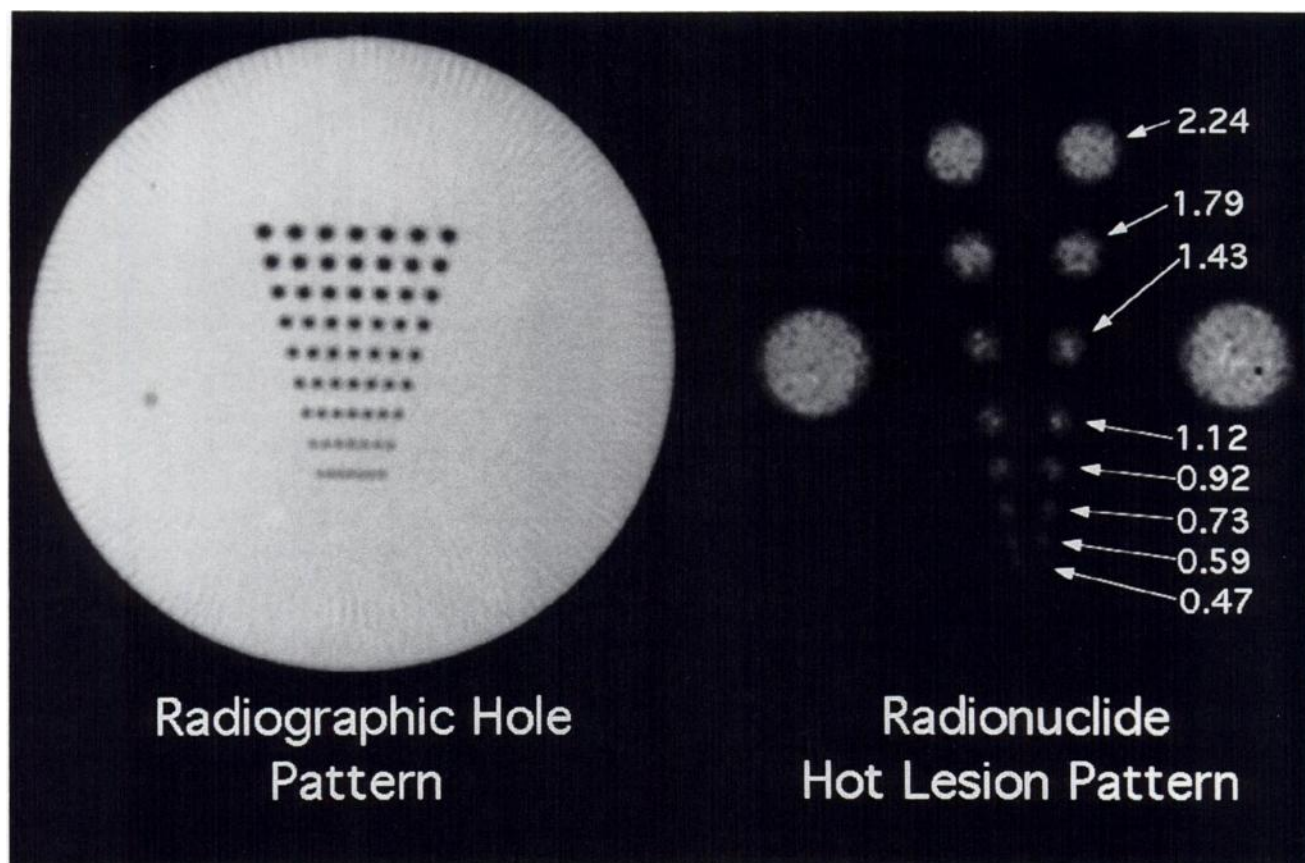


**FIGURE 5.** ETCT spatial resolution data. (Left) X-ray CT image of radiographic hole pattern. The holes in the top row have diameters and center-to-center spacings of 3.25 mm, and these decrease by 0.25-mm increments in subsequent rows. (Right) SPECT image of radionuclide hot lesion phantom. Diameters and center-to-center spacings for each pair of lesions are displayed in centimeters on the image.

pose the two images calculated the hue of each pixel in the overlaid image as a function of the intensity of the corresponding pixel in the SPECT image and its brightness as a function of the x-ray CT pixel. The degree of alignment displayed qualitatively in Figure 6 was a result of a direct overlay, with no preprocessing, of the two images acquired with the same detector and reconstructed with the same geometries.

Figure 7 qualitatively displays the results of pile-up correction on the simultaneously-acquired radionuclide data. The upper left figure shows the uncorrected SPECT sinogram and the figure beneath it shows the image reconstructed from this data using the ML-EM algorithm. Here, the radionuclide distribution reconstructs as a small perturbation on the pile-up background. The pairs of images shown in the middle and on the right respectively correspond to the pile-up-corrected data and the separately acquired data, which are displayed for comparison. The pile-up correction algorithm appears to recover, at the cost of reduced signal-to-noise ratio (SNR), much of the detail suppressed by pile-up in the simultaneously acquired SPECT sinogram data. This SNR loss is greatest at the edge of the sinogram, where the pile-up signal is largest, and decreases towards the center, where object attenuation

reduces the pile-up rate. This spatial dependence appears to hold for the reconstructed SPECT image as well, although we are currently performing studies to characterize the propagation of this noise through the ML-EM algorithm.

## DISCUSSION

SPECT has both obvious advantages and inherent disadvantages which affect its ability to image physiological function of the brain, the heart, tumors and other tissues and organ systems. It is relatively inexpensive, employs generator-produced radionuclides and is technically manageable in a medical center or community hospital. On the other hand, SPECT suffers from a range of problems, such as poor spatial resolution, limited photon statistics, poor anatomic localization and attenuation artifacts. These drawbacks affect the visual quality of SPECT images and limit the capability of SPECT to quantify physiological function.

By using the same detector to acquire both SPECT and x-ray CT data, the ETCT system has the potential of overcoming some of these limitations. Because of their ~1mm spatial resolution and vastly improved photon statistics ( $10^9$  versus  $10^7$  counts/slice), the x-ray CT images



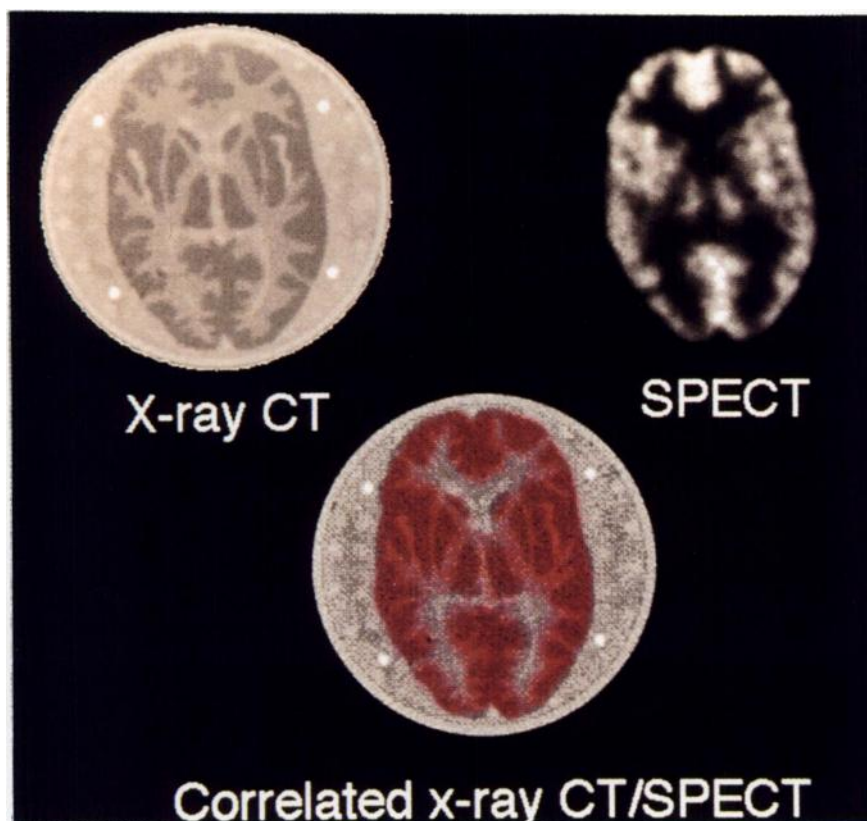


**FIGURE 6.** Images of a three-dimensional Hoffman brain phantom. (Upper left) X-ray CT image of phantom. The white spots visible in the acrylic regions are glue junctions. The phantom is contained within an external acrylic cylinder which holds the 19 acrylic brain slices. (Upper right) SPECT image of Hoffman brain phantom acquired with x-ray tube off. (Bottom) SPECT image in transparent color overlaid on correlated x-ray CT gray-scale image.

acquired with this device show improved definition of patient anatomy when compared to transmission images acquired with an external radionuclide source and a scintillation camera. The x-ray CT and SPECT images may be acquired simultaneously with the same detector array, permitting superposition of the SPECT image on the high-resolution x-ray CT map for improved localization. More-

over, preliminary results support the potential use of dual-energy x-ray CT to correct attenuation artifacts in the SPECT image by determining an accurate patient-specific attenuation map (9). Because of the anatomic heterogeneity of the thorax, these attenuation artifacts are most serious in measurements of myocardial perfusion (14). These errors, however, are also important for a variety of

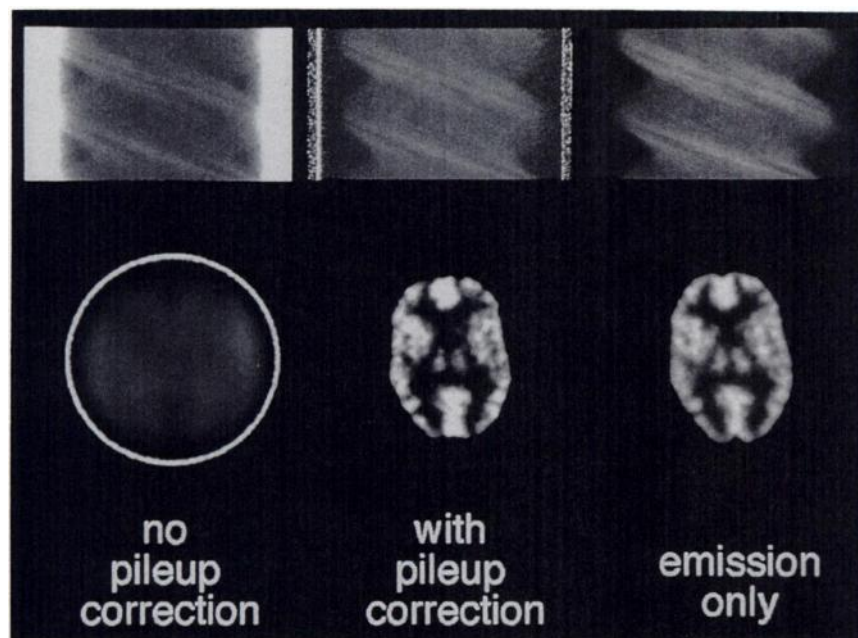


**FIGURE 7.** SPECT sinograms of Hoffman brain phantom displayed next to reconstructed images. (Upper left) Uncorrected sinogram showing effects of pulse pileup. (Lower left) Image reconstructed from uncorrected sinogram. (Upper middle) Pileup-corrected sinogram. (Lower middle) Image reconstructed from corrected sinogram. (Upper right) Sinogram of separately acquired SPECT data. (Lower right) Separately acquired SPECT image.

applications in other organ systems. Finally, the superior energy resolution of HPGe detectors permits improved scatter rejection when compared to sodium iodide, thus improving both qualitative contrast and quantitative accuracy in the radionuclide data. We plan to investigate this capability in future measurements.

Although the ETCT prototype has thus demonstrated a range of novel capabilities, there are technical limitations which affect our implementation of this technique. The primary technical limitation to simultaneous emission-transmission imaging using  $^{99m}\text{Tc}$  is posed by x-ray pile-up, which introduces spurious counts into the radionuclide data. Although it is possible to use the x-ray CT data to estimate and subtract the pile-up, the corrected SPECT image suffers a spatially variant loss in signal-to-noise which is maximized at the periphery of the image. We are now performing theoretical and experimental studies to quantify the noise introduced into the projection data, to characterize its propagation through the ML-EM algorithm and to estimate its severity for different clinical applications (e.g. brain and thoracic imaging). We are also evaluating possible solutions to this problem, one of which is to acquire the x-ray data at lower count rates, although we have not yet determined the level at which a lower count rate eliminates pile-up counts in the radionuclide window. Another promising solution is to employ a compensating x-ray filter which would have maximal thickness toward the outside of the patient, where the x-ray flux is maximum, and have minimal thickness toward the inside, where patient attenuation is highest. By reducing the x-ray count rate at the periphery of the object, this approach would reduce signal-to-noise problems caused by the pile-up subtraction. Finally, another technical limitation is that the use of low-energy radionuclides such as  $^{201}\text{Tl}$  would require that the emission and transmission measurements be performed sequentially rather than simultaneously. This would prolong the patient study and could lead to possible misregistration artifacts caused by patient motion.

While the work described above has revealed some of the novel capabilities and limitations of ETCT, the clinical implementation of this technique will depend on the availability of large two-dimensional HPGe arrays. Although two-dimensional segmentation of HPGe has been reported (15), these devices are hand-made and custom built. Ultimately, development of a practical clinical system will be driven by advances in HPGe fabrication techniques, by development of cost-effective readout technologies for large two-dimensional detector arrays and by advances in room temperature semiconductor detectors, such as ZnCdTe (16,17) and HgI (17).

## CONCLUSIONS

We have constructed a prototype ETCT imaging device and have demonstrated some of its capabilities and limitations. The system can perform both simultaneous and sequential SPECT and x-ray CT phantom studies. When

acquired simultaneously with x-ray CT data, the SPECT images must be corrected for x-ray pile-up, and the resultant SNR loss constitutes a possible limitation of the system. Because of its 4-hr image acquisition time, and the need to rotate the object being scanned, this prototype device is not suitable for patient scanning. Although the technology exists to build a practical detector array for whole-body studies, we will employ the current device to thoroughly characterize the fundamental capabilities and limitations of the ETCT technique before proceeding to that stage. Ultimately, such a device might allow SPECT images to be superimposed on x-ray CT maps for improved localization of radionuclide uptake.

## ACKNOWLEDGMENTS

The authors are grateful to Dr. Benjamin Tsui, Mr. Eric Frey and Mr. Chandrashekar Ramanathan of the University of North Carolina at Chapel Hill for providing the maximum-likelihood expectation-maximization software used to reconstruct the SPECT images in this project. The authors would like to thank Mr. Ed Chubak and Mr. Gus Gutierrez for technical support and Ms. Phyllis Bishoff for administrative support. We also thank Dr. Douglas Boyd, Dr. John Couch, Dr. Kristian Peschmann and Mr. Roger Schulte for illuminating and thoughtful discussions. This work was supported in part by grant 1R01CA50539 from the National Cancer Institute, grant 1P01DK39964 from the National Institute of Diabetes and Digestive and Kidney Diseases, and contract number NAG9-327 from the Johnson Space Flight Center (NASA). Mr. Gingold is supported by NIH pre-doctoral training grant NIH T6 6M08155.

## REFERENCES

1. Jaczak R, Coleman RE, Whitehead FR. Physical factors affecting quantitative measurements using gamma camera-based single photon emission computed tomography (SPECT). *IEEE Trans Nucl Sci* 1981;28:69-80.
2. Gould KL. Clinical cardiac positron emission tomography: state of the art. *Circulation* 1991;84:122-136.
3. Pelizzari CA, Chen GTY, Spelbring DR, Weichselbaum RR, Chen CT. Accurate three-dimensional registration of CT, PET and/or MR images of the brain. *J Comput Assist Tomogr* 1989;13:20-26.
4. Schad LR, Boesecke R, Schlegel W, et al. Three-dimensional image correlation of CT, MR and PET studies in radiotherapy treatment planning of brain tumors. *J Comput Assist Tomogr* 1987;11:948-954.
5. Fox PT, Perlmuter JS, Raichle ME. A stereotactic method of anatomical localization for positron emission tomography. *J Comput Assist Tomogr* 1985;9:141-153.
6. Holman BL, Zimmerman RE, Johnson KA, et al. Computer-assisted superimposition of magnetic resonance and high-resolution technetium-99m-HMPAO and thallium-201 SPECT imaging of the brain. *J Nucl Med* 1991;32:1478-1484.
7. Manglos SA, Bassano DA, Thomas FD. Cone-beam transmission for nonuniform attenuation compensation of SPECT images. *J Nucl Med* 1991;32:1813-1820.
8. Tsui BMW, Gullberg GT, Edgerton ER, et al. Correction of non-uniform attenuation in cardiac SPECT imaging. *J Nucl Med* 1989;30:497-507.
9. Lang TF, Hasegawa BH, Liew SC, et al. A prototype emission-transmission CT system. *Conf. Rec. IEEE Nucl Sci Symp* 1991;3:1902-1906.
10. Hasegawa BH, Gingold EL, Reilly SM, Liew SC, Cann CE. Description of a simultaneous emission-transmission CT system. *Proc SPIE* 1990;1231:50-60.
11. Hasegawa BH, Stebler B, Rutt BK, et al. A prototype high-purity germanium detector system with fast photon-counting circuitry for medical imaging. *Med Phys* 1991;18:900-909.
12. Ramachandran GN, Lakshminarayanan AV. Three-dimensional reconstruction from radiographs and electron micrographs: applications of con-

- volution instead of Fourier Transforms. *Proc Natl Acad Sci USA* 1971; 68:2236–2240.
13. Kak AC, Slaney M. *Principles of computerized tomographic imaging*. New York: IEEE Press; 1988:75–77.
  14. Bonow RO, Berman DS, Gibbons RG, et al. Cardiac positron emission tomography. *Circulation* 1991;84:447–454.
  15. Gutknecht D. Photomask technique for fabricating high purity germanium strip detectors. *Nucl Instrum Meth* 1990;A288:13–18.
  16. Entine G, Waer P, Tiernan T, Squillante MR. Survey of CdTe nuclear detector applications. *Nucl Instrum Meth* 1989;A283:282–290.
  17. Barber HB, Barrett HH, Hickernell TS, Kwo DP, et al. *Med Phys* 1991; 18:373–381.